J. Fluid Mech. (2017), *vol.* 818, *pp.* 100–115.
doi:10.1017/jfm.2017.138

Dynamics of an elastic sphere containing a thin creeping region and immersed in an acoustic region for similar viscous-elastic and acoustic time and length scales

Yonatan Friedman[1] **and Amir D. Gat**[1,†]

[1]Faculty of Mechanical Engineering, Technion – Israel Institute of Technology, Haifa 3200003, Israel

(Received 1 August 2016; revised 28 February 2017; accepted 1 March 2017;
first published online 29 March 2017)

The characteristic time of low-Reynolds-number fluid–structure interaction scales linearly with the ratio of fluid viscosity to solid Young's modulus. For sufficiently large values of Young's modulus, both time and length scales of the viscous-elastic dynamics may be similar to acoustic time and length scales. However, the requirement of dominant viscous effects limits the validity of such regimes to micro-configurations. We here study the dynamics of an acoustic plane wave impinging on the surface of a layered sphere, immersed within an inviscid fluid, and composed of an inner elastic sphere, a creeping fluid layer and an external elastic shell. We focus on configurations with similar viscous-elastic and acoustic time and length scales, where the viscous-elastic speed of interaction between the creeping layer and the elastic regions is similar to the speed of sound. By expanding the linearized spherical Reynolds equation into the relevant spectral series solution for the hyperbolic elastic regions, a global stiffness matrix of the layered elastic sphere was obtained. The maximal pressure difference induced by the acoustic wave on the creeping region was found to occur for identical viscous-elastic and acoustic length scales. Comparing an elastic sphere with an embedded creeping layer to a fully elastic sphere, a significant reduction in magnitude and fluctuations (with regard to wavelength) are observed for both the displacements of the solid and target strength of the sphere. This effect was most significant for identical viscous-elastic and acoustic time scales. This work relates viscous-elastic dynamics to acoustic scattering and may pave the way to the design of novel metamaterials with unique acoustic properties.

Key words: acoustics, low-Reynolds-number flows, micro-/nano-fluid dynamics

1. Introduction

In this work we examine the dynamics of an elastic sphere with an embedded viscous layer, excited by an impinging acoustic plane wave. We focus on configurations with similar acoustic and viscous-elastic time scales as well as acoustic wavelengths comparable with the sphere radius. The characteristic time scale of the linearized interaction between an elastic structure and a creeping flow scales as $\propto \mu/y$ (e.g.

† Email address for correspondence: amirgat@technion.ac.il

Elbaz & Gat 2014) where the relevant Womersley number scales as $\propto \rho r^2 y/\mu^2$ (y is Young's modulus, μ is viscosity, r is characteristic length and ρ is density). Thus, the characteristic time scale of the viscous-elastic interaction can be reduced, without increasing inertial effects, by decreasing r^2/μ inversely with μ/y. For geometries in the micrometre scale, fluid–structure interaction at the creeping regime may occur at time scales similar to the acoustic time scale r/c, where c is the speed of sound.

Transient and oscillatory viscous-elastic interaction dynamics are relevant to various fields (Duprat & Stone 2015). Among these are biological configurations such as propulsion of micro-organisms by flagella (Wiggins & Goldstein 1998; Camalet & Jülicher 2000; Tony, Lauga & Hosoi 2006), analysis and testing of corneal biomechanics (Chauhan & Radke 2002; Duchemin & Vandenberghe 2014; Han *et al.* 2014) and flows in small blood vessels (Lowe & Pedley 1995; Heil 1997; Canic & Mikelic 2003). Other relevant fields are geophysical gravity currents involving elastic surfaces (Balmforth, Craster & Hewitt 2015; Hewitt, Balmforth & De Bruyn 2015), elastic peeling problems (McEwan & Taylor 1966; Hosoi & Mahadevan 2004; Lister, Peng & Neufeld 2013) and applications such as viscous-elastic pumps for the creeping flow regime (Arco *et al.* 2014).

The subject of an acoustic plane wave impinging on an elastic spherical configuration has been studied extensively (e.g. Love 1927; Faran 1951; Logan 1965). A common interest in such problems is acoustic scattering (Bowen & Urzhumov 2016), which defines the target strength of the sphere and is of importance to applications such as ultrasound tests, tomography and seismology. Various previous studies examined embedded layers as a mechanism to achieve a desired reduction of target strength of a spherical configuration. These include Guild, Alu & Haberman (2011), who studied the effect of a single metamaterial layer and showed a target strength reduction of up to 30 dB for specific frequencies. In a later study Guild *et al.* (2015) examined the effect of spherical fluid layers surrounding non-spherical elastic structures, and obtained a reduction of 30–40 dB in scattering strength. Torrent & Sánchez-Dehesa (2008) have proposed to use a large number of alternating metamaterial layers, and later Huang, Zhong & Liu (2014) have extended this approach to include turbulent flow, with moderate success. Analysis of acoustic scattering from spherical configurations with an embedded viscous layer is presented in Skelton & James (1997). However, due to an initial assumption of P-waves propagating within the fluidic layer, and since viscosity is represented only as a damping mechanism to these waves, the mathematical treatment of Skelton & James (1997) could not be extended to the creeping regime, which is governed by the relevant Reynolds equation.

In this context, the goal of the current work is to study the interaction between viscous-elastic dynamics and acoustic waves, for micro-configurations with similar viscous-elastic and acoustic time and length scales. This requires extension of the analysis of a spherical layered elastic structure and incorporation of the parabolic Reynolds equation into the spectral series solution for the hyperbolic elastic and acoustic regions. The structure of this work is as follows. In § 2 we define the problem, apply order-of-magnitude analysis and develop the Reynolds equation to a series of Legendre polynomials. In § 3 we develop the spectral stiffness matrix for the creeping fluidic layer and incorporate it into the global stiffness matrix of the elastic sphere. In § 4 we present and discuss the pressure and velocity within the fluidic layer, as well as the effect of the viscous layer on the displacements and target strength of the sphere. In § 5 we give concluding remarks.

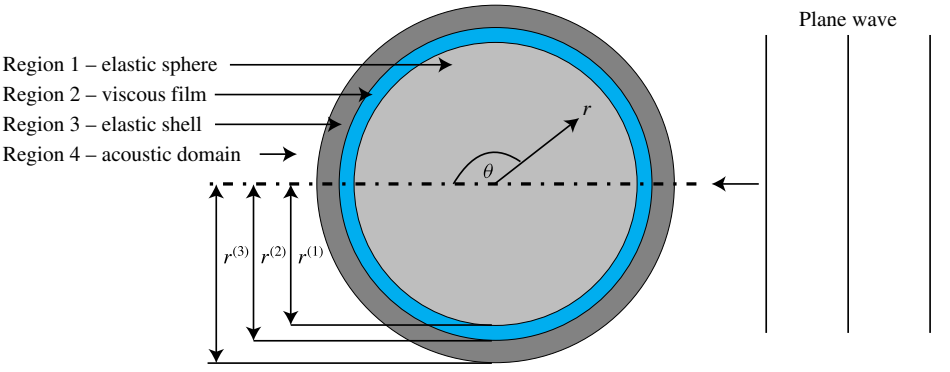

FIGURE 1. (Colour online) Illustration of the layered sphere, the coordinate system and the impinging acoustic wave.

2. Problem formulation and order-of-magnitude analysis

We examine an acoustic wave interacting with a core-in-shell geometry consisting of an elastic sphere surrounded by thin viscous and elastic layers. In order to examine configurations with significant spatial pressure variation, we focus on acoustic wavelengths similar to the radius of the sphere. The configuration is illustrated in figure 1 and contains four regions: region 1 ($r \leqslant r^{(1)}$) is an inner elastic sphere; region 2 ($r^{(1)} < r \leqslant r^{(2)}$) is a thin viscous layer with negligible inertial effects; region 3 ($r^{(2)} < r \leqslant r^{(3)}$) is an elastic spherical shell; and region 4 ($r^{(3)} < r$) is an acoustic region with negligible viscous effects. We examine micro-configurations where the characteristic time scale of viscous-elastic interaction is similar to the time scale of the acoustic wave.

We employ a spherical coordinate system, denoted by (θ, ϕ, r), with origins located at the centre of the sphere at rest. Time is denoted by t. The velocity of the acoustic wave is parallel to the $\phi = \theta = 0$ direction and thus the configuration is axisymmetric with regard to the $\phi = \theta = 0$ line. The displacements and velocity in region M are defined by $\boldsymbol{d}^{(M)} = (d_r^{(M)}, d_\theta^{(M)})$ and $\boldsymbol{u}^{(M)} = (u_r^{(M)}, u_\theta^{(M)})$, respectively, where $\boldsymbol{u}^{(M)} = \partial \boldsymbol{d}^{(M)}/\partial t$. Stress in region M is denoted by $\sigma_{jk}^{(M)}$, where the stress is in the j-direction and acts on the plane perpendicular to the k-direction. Density is denoted by $\rho^{(M)}$. In the fluidic regions ($M = 2, 4$) we denote pressure as $p^{(M)}$. The pressure amplitude of the acoustic wave in region 4 is denoted by p_a, the acoustic wavelength is denoted by l and the speed of sound is $c^{(M)}$.

The Newtonian fluidic layers are governed by Navier–Stokes equations, while the linearly elastic regions are governed by the Cauchy–Navier equations. For all regions, conservation of mass,

$$\frac{\partial \rho^{(M)}}{\partial t} + \nabla \cdot (\rho^{(M)} \boldsymbol{u}^{(M)}) = 0, \tag{2.1}$$

and conservation of momentum (neglecting body forces),

$$\rho^{(M)} \frac{\mathrm{D}\boldsymbol{u}^{(M)}}{\mathrm{D}t} = \nabla \cdot \bar{\boldsymbol{\sigma}}^{(M)}, \tag{2.2}$$

are applied, where $\bar{\boldsymbol{\sigma}}^{M}$ is the stress tensor. In the fluidic regions ($M = 2, 4$) the constitutive relation is given by

$$\bar{\boldsymbol{\sigma}}^{(M)} = \mu^{(M)}[\nabla \boldsymbol{u}^{(M)} + (\nabla \boldsymbol{u}^{(M)})^t] + [p^{(M)} - (\tfrac{2}{3}\mu^{(M)} - \lambda^{(M)})(\nabla \cdot \boldsymbol{u}^{(M)})]\bar{\boldsymbol{I}}, \tag{2.3}$$

where $p = -\mathrm{tr}(\bar{\boldsymbol{\sigma}}^{(M)})/3$, while in the elastic layers ($M = 1, 3$) (Howell, Kozyreff & Ockendon 2009)

$$\bar{\boldsymbol{\sigma}}^{(M)} = \mu^{(M)}[\nabla \boldsymbol{d}^{(M)} + (\nabla \boldsymbol{d}^{(M)})^t) + \lambda^{(M)}(\nabla \cdot \boldsymbol{d}^{(M)})\bar{\boldsymbol{I}}. \tag{2.4}$$

For the fluidic regions ($M = 2, 4$) $\mu^{(M)}$ and $\lambda^{(M)}$ are the shear and bulk viscosity coefficients, respectively. For the elastic regions ($M = 1, 3$) $\lambda^{(M)}$ and $\mu^{(M)}$ are the Lamé constants, given by

$$\mu^{(M)} = \frac{y^{(M)}}{2(1+\nu^{(M)})} \tag{2.5a}$$

and

$$\lambda^{(M)} = \frac{y^{(M)}\nu^{(M)}}{(1+\nu^{(M)})(1-2\nu^{(M)})}, \tag{2.5b}$$

where $y^{(M)}$ is Young's elastic modulus and $\nu^{(M)}$ is Poisson's ratio. In addition, we require the fluid in region 2 to be governed by interaction between fluid viscosity and the elasticity of the bounding regions (1, 3), and thus assume negligible compressibility effects, $\rho^{(2)} = \mathrm{const}$.

Our analysis examines configurations that agree with the following small geometric parameters, representing the ratio between the width of the viscous layer and the radius of the inner sphere,

$$\varepsilon^{(2)} = \frac{r^{(2)} - r^{(1)}}{r^{(1)}} \ll 1, \tag{2.6a}$$

and the width of the elastic shell layer to the radius of the inner sphere

$$\varepsilon^{(3)} = \frac{r^{(3)} - r^{(2)}}{r^{(1)}} \ll 1. \tag{2.6b}$$

In addition, we focus on the acoustic pressure field, which is significantly non-uniform across the surface of the sphere. This sets the characteristic acoustic wavelength in region 4 to $\sim O(r^{(1)})$ and thus the characteristic acoustic time scale is $t_a = r^{(1)}/c^{(4)}$. We denote t^* as the characteristic viscous-elastic time scale and (d_r^*, d_θ^*) are characteristic displacements of the elastic regions. The geometric requirements (2.6) are thus supplemented by the physical requirements of similar viscous-elastic and acoustic time scales,

$$t^* \sim t_a = \frac{r^{(1)}}{c^{(4)}}, \tag{2.7a}$$

small elastic displacements,

$$\frac{d_r^*}{r^{(1)}}, \frac{d_\theta^*}{r^{(1)}} \ll 1, \tag{2.7b}$$

negligible inertia in region 2,

$$(\alpha^{(2)})^2 = \frac{\rho^{(2)}(r^{(2)} - r^{(1)})^2}{\mu^{(2)} t^*} \ll 1, \tag{2.7c}$$

and negligible viscosity in region 4,

$$(\alpha^{(4)})^2 = \frac{\rho^{(4)}(r^{(1)})^2}{\mu^{(4)} t_a} \gg 1, \tag{2.7d}$$

where $(\alpha^{(2)})^2$ and $(\alpha^{(4)})^2$ denote the Womersley numbers in regions 2 and 4, respectively.

We apply order-of-magnitude analysis in order to quantify the physical requirements described in (2.7) in terms of material properties and geometric parameters of the layered sphere. Hereafter normalized variables are denoted by capital letters and characteristic values are denoted by superscript asterisks.

We define the normalized radial coordinate and time,

$$R = \frac{r}{r^{(1)}}, \quad T = \frac{t}{t^*}, \tag{2.8a,b}$$

and the normalized velocity and pressure of region 2,

$$(U_\theta^{(2)}, U_r^{(2)}) = \left(\frac{u_\theta^{(2)}}{u_\theta^{(2),*}}, \frac{u_r^{(2)}}{u_r^{(2),*}} \right), \quad P^{(2)} = \frac{p^{(2)}}{p_a}, \tag{2.9a,b}$$

where $(u_r^{(2),*}, u_\theta^{(2),*})$ is the characteristic speed in region 2. The normalized displacements of the elastic boundaries of region 2 are

$$(D_r^{(1)}, D_\theta^{(1)}) = \left(\frac{d_r^{(1)}(r = r^{(1)})}{d_r^*}, \frac{d_\theta^{(1)}(r = r^{(1)})}{d_\theta^*} \right) \tag{2.10}$$

and

$$(D_r^{(2)}, D_\theta^{(2)}) = \left(\frac{d_r^{(2)}(r = r^{(2)})}{d_r^*}, \frac{d_\theta^{(2)}(r = r^{(2)})}{d_\theta^*} \right). \tag{2.11}$$

The characteristic fluid velocity, solid displacement and viscous-elastic time scale may be estimated by substituting (2.8)–(2.11) into (2.1)–(2.4) and applying order-of-magnitude analysis. From the governing equations of the creeping region 2, we obtain

$$u_\theta^{(2),*} \sim \frac{p_a(\varepsilon^{(2)})^2 r^{(1)}}{\mu^{(2)}}, \quad u_r^{(2),*} \sim \varepsilon^{(2)} u_\theta^{(2),*}, \quad t^* \sim \frac{d_r^*}{u_r^{(2),*}} \tag{2.12a–c}$$

and

$$\sigma_{r\theta}^{(3),*} \sim \mu^{(2)} \frac{u_\theta^{(2),*}}{\varepsilon^{(2)} r^{(1)}}, \quad \sigma_{rr}^{(3),*} = p_a. \tag{2.13a,b}$$

Order-of-magnitude analysis of the governing equations of the elastic region 3, and specifically (2.4), yields

$$d_\theta^* \sim \frac{p_a r^{(1)}}{\lambda^{(3)}}, \quad d_r^* \sim \frac{p_a r^{(1)}}{\varepsilon^{(2)} \lambda^{(3)}}, \quad t^* \sim \frac{\mu^{(2)}}{(\varepsilon^{(2)})^3 \varepsilon^{(3)} \lambda^{(3)}} \tag{2.14a–c}$$

and

$$\sigma_{r\theta}^{(3),*} \sim p_a \varepsilon^{(2)}, \quad \sigma_{\theta\theta}^{(3),*} \sim \frac{p_a}{\varepsilon^{(3)}}. \tag{2.15a,b}$$

Applying (2.7) and substituting (2.8)–(2.11) into (2.1)–(2.3), the leading-order normalized governing equation for region 2 is the relevant linearized Reynolds equation,

$$\frac{1}{\sin\theta}\frac{\partial}{\partial\theta}\left(\sin\theta\frac{\partial P^{(2)}}{\partial\theta}\right) \sim 12\left(\frac{\partial D_r^{(2)}}{\partial T} - \frac{\partial D_r^{(1)}}{\partial T}\right) + \frac{6}{\sin\theta}\frac{\partial}{\partial\theta}\left[\sin\theta\left(\frac{\partial D_\theta^{(2)}}{\partial T} + \frac{\partial D_\theta^{(1)}}{\partial T}\right)\right]. \tag{2.16}$$

From (2.12)–(2.15), we can relate our physical requirements (2.7) to the geometric and material properties of the configuration. These include the requirements of similar viscous-elastic and acoustic time scales,

$$\frac{\mu^{(2)}c^{(4)}}{(\varepsilon^{(2)})^3\varepsilon^{(3)}\lambda^{(3)}r^{(3)}} \sim O(1), \tag{2.17a}$$

small deformations,

$$\frac{p_a}{\varepsilon^{(3)}\lambda^{(3)}} \ll 1, \tag{2.17b}$$

negligible inertial effects in region 2,

$$(\alpha^{(2)})^2 = \frac{\rho^{(2)}(\varepsilon^{(2)})^5\varepsilon^{(3)}\lambda^{(3)}(r^{(1)})^2}{(\mu^{(2)})^2} \ll 1, \tag{2.17c}$$

and negligible viscous effects in region 4

$$(\alpha^{(4)})^2 = \frac{\rho^{(4)}r^{(3)}c^{(4)}}{\mu^{(4)}} \gg 1. \tag{2.17d}$$

The requirements of small deformation in region 3 (2.17*b*) and negligible inertial effects in region 4 (2.17*d*) are easily satisfied for a wide range of common geometric configurations and material properties. However, the requirement of negligible inertial effects in region 2 (2.17*c*) combined with the requirement of similar acoustic and viscous-elastic time scales (2.17*a*) severely limits the range of validity of the current analysis. Even for highly viscous fluids (e.g. silicone oil with $\mu^{(2)} \approx 100$ Pa s) and rigid solids (e.g. steel with $y^{(3)} = 200$ GPa and $\nu^{(3)} = 0.29$) surrounded by water ($\rho^{(4)} = 1000$ kg m^{-3} and $c^{(4)} = 1484$ m s^{-1}), the above requirements limit the sphere diameter to $2r^{(1)} \leqslant 2$ mm and thus to ultrasound frequencies $\geqslant 750$ kHz. In addition, since $(r^{(2)} - r^{(1)})/r^{(1)} \ll 1$, the results are practically valid only for microfluidic configurations where $r^{(2)} - r^{(1)} \approx 100$ μm or less.

3. Incorporating the Reynolds equation into the acoustic stiffness matrix

Acoustic scattering of plane waves from spherical configurations has been studied extensively, and the treatment of regions 1, 3 and 4 may be found elsewhere (e.g. Love 1927; Logan 1965; Skelton & James 1997) and will be omitted here. The aim of this section is the incorporation of the parabolic region 2 into the standard scheme

for the hyperbolic elastic and acoustic regions. In spherical coordinates, the impinging plane wave in region 4, denoted by $P_i^{(4)} = p_i^{(4)}/p_a$, is given by

$$P_i^{(4)} = \sum_{n=0}^{\infty} i^n (2n+1) \mathrm{j}_n(kr) L_n(\cos\theta). \tag{3.1}$$

where $k = \omega/c^{(4)}$ is the impinging wavenumber, L_n is Legendre polynomial and j_n is the spherical Bessel function of the first kind.

The total scattered pressure in the external acoustic fluid, denoted by $P_s^{(4)} = P_r^{(4)} + P_e^{(4)}$, can be presented as the sum of the pressure reflected from a rigid sphere, $P_r^{(4)}$, and the additional pressure due to elastic displacements of the sphere, $P_e^{(4)}$ (all pressures are scaled by p_a). The acoustic scattering due to a rigid sphere, given by $P_r^{(4)} = p_r^{(4)}/p_a$, is

$$P_r^{(4)} = -\sum_{n=0}^{\infty} i^n (2n+1) \mathrm{j}_n(kr) \frac{\mathrm{j}_n'(kr^{(3)})}{\mathrm{h}_n'(kr^{(3)})} \mathrm{h}_n(kr^{(3)}) L_n(\cos\theta), \tag{3.2}$$

where h_n is the spherical Hankel function of the first kind.

We thus hereafter focus on calculation of acoustic scattering due to elastic displacements of the sphere $P_e^{(4)}$. In order to incorporate the dynamics of the Reynolds equation governing region 2 (2.16) into the calculation of $P_e^{(4)}$, we require series solution of the radial displacements and stress on the boundaries of region 2 to be of the form

$$(D_R^{(1)}, D_R^{(2)}, S_{RR}^{(1)}, S_{RR}^{(2)}) = \mathrm{e}^{\mathrm{i}\Omega T} \sum_{n=0}^{\infty} L_n(\cos\theta)(D_{R,n}^{(1)}, D_{R,n}^{(2)}, S_{R\theta,n}^{(1)}, S_{R\theta,n}^{(2)}), \tag{3.3a}$$

where $D_R^{(1)}$ and $D_R^{(2)}$ are amplitudes of radial displacements at $R = R^{(1)}$ and $R = R^{(2)}$, respectively. Similarly, $S_{RR}^{(1)}$ and $S_{RR}^{(2)}$ are amplitudes of radial stress at $R = R^{(1)}$ and $R = R^{(2)}$, respectively. In addition, we require series solution of the tangential displacements and stress on the boundaries of region 2 to be of the form

$$(D_\theta^{(1)}, D_\theta^{(2)}, S_{R\theta}^{(1)}, S_{R\theta}^{(2)}) = \mathrm{e}^{\mathrm{i}\Omega T} \sum_{n=0}^{\infty} \frac{\partial L_n(\cos\theta)}{\partial\theta}(D_{\theta,n}^{(1)}, D_{\theta,n}^{(2)}, S_{RR,n}^{(1)}, S_{RR,n}^{(2)}), \tag{3.3b}$$

where $D_\theta^{(1)}$ and $D_\theta^{(2)}$ are amplitudes of displacements in the θ-direction at $R = R^{(1)}$ and $R = R^{(2)}$, respectively. The parameters $S_{R\theta}^{(1)}$ and $S_{R\theta}^{(2)}$ are amplitudes of shear stress at $R = R^{(1)}$ and $R = R^{(2)}$, respectively.

In the examined limit of incompressible lubrication flow, the pressure in region 2 is independent of r, and applying (3.3a) yields a general solution in terms of the orthogonal Legendre polynomials

$$P^{(2)}(\theta) = \sum_{n=0}^{\infty} P_n^{(2)} L_n(\cos(\theta)), \tag{3.4}$$

where $P_n^{(2)}$ are constants representing the pressure amplitude of each Legendre mode. Substituting (3.3) and (3.4) into (2.16) and utilizing the identity

$$\frac{1}{\sin(\theta)} \frac{\partial}{\partial\theta} \left(\sin(\theta) \frac{\partial L_n(\cos(\theta))}{\partial\theta} \right) = n(n+1) L_n(\cos(\theta)) \tag{3.5}$$

yields $P_n^{(2)}$,

$$P_n^{(2)} = \mathrm{i}\Omega \left[\frac{12}{n(n+1)} (D_{R,n}^{(2)} - D_{R,n}^{(1)}) + 6(D_{\theta,n}^{(2)} + D_{\theta,n}^{(1)}) \right], \tag{3.6}$$

and $U_{\theta,n}^{(2)}$ can be obtained from the tangential momentum equation,

$$U_{\theta,n}^{(2)} = \mathrm{e}^{\mathrm{i}\Omega T} \frac{\partial L_n(\cos(\theta))}{\partial \theta} \left[P_n^{(2)} \frac{H(H-1)}{2} + D_{\theta,n}^{(1)} + H(D_{\theta,n}^{(2)} - D_{\theta,n}^{(1)}) \right], \tag{3.7}$$

where $H = (r - r^{(1)})/(r^{(2)} - r^{(1)})$. Since substitution of (3.6) into the lubrication equation (2.16) yields $u_\theta^{(2)}$ and $\sigma_{r\theta}^{(2)}$ to be series of the derivatives of Legendre polynomials, the series representation of region 2 agrees with the requirements of both (3.3*a*) and (3.3*b*). Thus we can proceed and incorporate parabolic region 2 into the acoustic scheme for the hyperbolic regions 1, 3 and 4.

Hereafter we revert to dimensional parameters. Applying the leading-order lubrication relations $p^{(2)} \sim \sigma_{rr}^{(2)}$ and $\sigma_{r\theta}^{(2)} \sim \mu^{(2)} \partial u_\theta^{(2)}/\partial r$, we can obtain from (3.6) and (3.7) a relation between the traction vector $\boldsymbol{s}_n = [\sigma_{rr,n}^{(1)}, \sigma_{r\theta,n}^{(1)}, \sigma_{rr,n}^{(3)}, \sigma_{r\theta,n}^{(3)}]$ created by excitation of the form of Legendre polynomial of order n and the displacement vector $\boldsymbol{d}_n = [d_{r,n}^{(1)}, d_{\theta,n}^{(1)}, d_{r,n}^{(3)}, d_{\theta,n}^{(3)}]$ on the boundaries of region 2. This yields $\{\boldsymbol{d}_n\} = [v_{ij}]^{-1}\{\boldsymbol{s}_n\}$, where v_{ij} is the dimensional stiffness matrix for the Reynolds region 2 given by

$$v_{ij,n} = \begin{bmatrix} \dfrac{12\mu^{(2)}\mathrm{i}\omega}{(\varepsilon^{(2)})^3 r^{(1)} n(n+1)} & -\dfrac{6\mu^{(2)}\mathrm{i}\omega}{(\varepsilon^{(2)})^2 r^{(1)}} & -\dfrac{12\mu^{(2)}\mathrm{i}\omega}{(\varepsilon^{(2)})^3 r^{(1)} n(n+1)} & -\dfrac{6\mu^{(2)}\mathrm{i}\omega}{(\varepsilon^{(2)})^2 r^{(1)}} \\ \dfrac{6\mu^{(2)}\mathrm{i}\omega}{(\varepsilon^{(2)})^2 r^{(1)} n(n+1)} & -\dfrac{4\mu\mathrm{i}\omega}{\varepsilon^{(2)} r^{(1)}} & -\dfrac{6\mu^{(2)}\mathrm{i}\omega}{(\varepsilon^{(2)})^2 r^{(1)} n(n+1)} & -\dfrac{2\mu\mathrm{i}\omega}{\varepsilon^{(2)} r^{(1)}} \\ \dfrac{12\mu^{(2)}\mathrm{i}\omega}{(\varepsilon^{(2)})^3 r^{(1)} n(n+1)} & -\dfrac{6\mu^{(2)}\mathrm{i}\omega}{(\varepsilon^{(2)})^2 r^{(1)}} & -\dfrac{12\mu^{(2)}\mathrm{i}\omega}{(\varepsilon^{(2)})^3 r^{(1)} n(n+1)} & -\dfrac{6\mu^{(2)}\mathrm{i}\omega}{(\varepsilon^{(2)})^2 r^{(1)}} \\ -\dfrac{6\mu^{(2)}\mathrm{i}\omega}{(\varepsilon^{(2)})^2 r^{(1)} n(n+1)} & \dfrac{2\mu^{(2)}\mathrm{i}\omega}{\varepsilon^{(2)} r^{(1)}} & \dfrac{6\mu^{(2)}\mathrm{i}\omega}{(\varepsilon^{(2)})^2 r^{(1)} n(n+1)} & \dfrac{4\mu^{(2)}\mathrm{i}\omega}{\varepsilon^{(2)} r^{(1)}} \end{bmatrix}. \tag{3.8}$$

A global spectral matrix of the tractions and the displacements for Legendre mode n, connecting Reynolds region 2 to regions 1, 3 and 4, may now be obtained,

$$\begin{bmatrix} d_{r,n}^{(3)} \\ d_{\theta,n}^{(3)} \\ d_{r,n}^{(2)} \\ d_{\theta,n}^{(2)} \\ d_{r,n}^{(1)} \\ d_{\theta,n}^{(1)} \end{bmatrix} = \begin{bmatrix} e_{11}+f_{11} & e_{12} & e_{13} & e_{14} & 0 & 0 \\ e_{21} & e_{22} & e_{23} & e_{24} & 0 & 0 \\ e_{31} & e_{32} & e_{33}+v_{11} & e_{34}+v_{12} & v_{13} & v_{14} \\ e_{41} & e_{42} & e_{43}+v_{21} & e_{44}+v_{22} & v_{23} & v_{24} \\ 0 & 0 & v_{31} & v_{32} & v_{33}+g_{11} & v_{34}+g_{12} \\ 0 & 0 & v_{41} & v_{42} & v_{43}+g_{21} & v_{44}+g_{22} \end{bmatrix}_{,n}^{-1} \begin{bmatrix} \sigma_{rr,n}^{(3)} \\ 0 \\ 0 \\ 0 \\ 0 \\ 0 \end{bmatrix}, \tag{3.9}$$

where $\sigma_{rr,n}^{(3)} = -p_a i^{n+1}(2n+1)(c^{(4)})^2/\omega^2 r^{(3)} h_n'(r^{(3)}\omega/c^{(4)})$ is the stress applied by the impinging plane wave. The coefficients for the acoustic region 4 and the elastic regions 1 and 3 are presented in the Appendix and their derivation may be obtained from Skelton & James (1997). Specifically, f_{11} is defined in (A 1), $\boldsymbol{e}$ is defined in (A 2) and $\boldsymbol{g}$ is defined in (A 23).

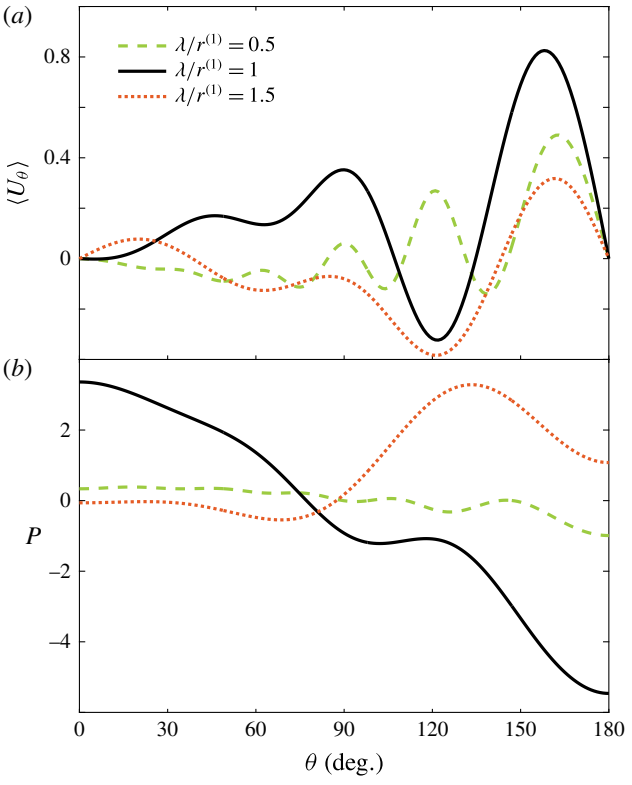

FIGURE 2. (Colour online) Normalized pressure and r-averaged velocity in region 2. (a) Distribution of the r-averaged speed in the θ-direction $\langle U_\theta \rangle$. (b) Pressure P angle θ for $\lambda = 0.5r^{(1)}$ (green dashed), $\lambda = r^{(1)}$ (black full) and $\lambda = 1.5r^{(1)}$ (red dotted). In all cases $\mu^{(2)}c^{(4)}/(\varepsilon^{(2)})^3\varepsilon^{(3)}\lambda^{(3)}r^{(1)} = 1$. As expected, $\lambda = r^{(1)}$ exhibits the most variance in fluidic pressure and the characteristic length scale of the induced velocity is similar to the external wavelength.

Mode $n = 0$ corresponds to spatially uniform pressure in region 4, for which the stiffness matrix of region 2 ($v_{ij,n}$) and thus the global stiffness matrix (3.10) are singular. This singularity expresses the trivial solution for the fluid θ-direction momentum conservation equation. Resolving this requires directly applying mass conservation to region 2, yielding $d^{(1)}_{r,n=0} = d^{(2)}_{r,n=0}$ combined with symmetry requirements $d^{(3)}_{\theta,n=0} = d^{(2)}_{\theta,n=0} = d^{(1)}_{\theta,n=0} = 0$. The resulting simplified system of equations for the displacements for $n = 0$ is

$$\begin{bmatrix} d^{(3)}_{r,n=0} \\ d^{(2)}_{r,n=0} \end{bmatrix} = \begin{bmatrix} e_{11} + f_{11} & e_{13} \\ e_{21} & e_{23} \end{bmatrix}^{-1}_{n=0} \begin{bmatrix} \sigma^{(3)}_{rr,n=0} \\ 0 \end{bmatrix}. \tag{3.10}$$

4. Results and comparison to a fully elastic sphere

Figure 2 presents the velocity and pressure fields in region 2 due to the impinging acoustic plane wave. In order to comply with the physical requirements described in (2.17a), the examined configuration consists of highly rigid elastic regions 1 and 3 (steel with $y^{(1)} = y^{(3)} = 200$ GPa, $\nu^{(1)} = \nu^{(3)} = 0.29$) and the embedded viscous film

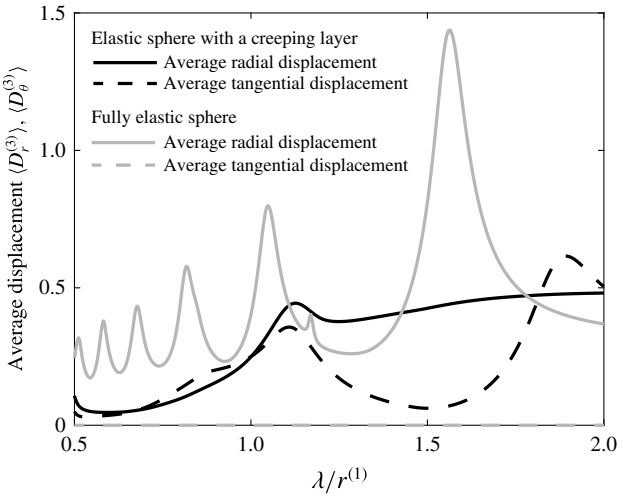

FIGURE 3. Normalized average displacements in the θ- and r-directions ($\langle D_\theta^{(3)} \rangle$ and $\langle D_r^{(3)} \rangle$, respectively) versus the normalized wavelength $\lambda/r^{(1)}$.

of region 2 is a highly viscous silicone oil ($\rho^{(2)} = 970$ kg m^{-3}, $\mu^{(2)} = 100$ Pa s). The geometry of the layered sphere is defined by $r^{(1)} = 0.6$ mm, $r^{(2)} = 1.2r^{(1)}$ and $r^{(3)} = 1.4r^{(1)}$. The sphere is submerged in water ($\rho^{(4)} = 1000$ kg m^{-3}, $\mu^{(4)} = 10^{-3}$ Pa s) with speed of sound of $c^{(4)} = 1480$ m s^{-1}.

Figure 2(a) presents the r-averaged speed in the θ-direction $\langle U_\theta \rangle$, defined by

$$\langle U_\theta \rangle = \int_{R^{(1)}}^{R^{(2)}} U(R, \theta)\, \mathrm{d}R, \tag{4.1}$$

for impinging wavelengths of $\lambda/r^{(1)} = 0.5$ (green dashed line), 1 (black full line) and 1.5 (red dotted line). In all cases, the magnitude of the average speed, induced due to both the pressure gradient and the elastic displacements of the boundaries in the θ-direction, is maximal near $\theta \approx 160°$. The density of the velocity peaks increases inversely with $\lambda/r^{(1)}$ and, while $\lambda/r^{(1)} = 1$ yields the maximal values of $\langle U_\theta \rangle$, all wavelengths yield speeds with similar order of magnitude.

Figure 2(b) presents the pressure in region 2 versus θ for identical wavelengths as in figure 2(a) ($\lambda/r^{(1)} = 0.5$, 1 and 1.5). Similarly to $\langle U_\theta \rangle$, the pressure increases in the direction in which the wave impinges on the surface of the sphere. Unlike figure 2(a), an order-of-magnitude difference in the characteristic pressure is evident for $\lambda/r^{(1)} = 0.5$ compared to $\lambda/r^{(1)} = 1.5$, representing a smaller effective length scale in the θ-direction (see (2.12)). The maximal pressure difference within the creeping layer occurs for $\lambda/r^{(1)} = 1$, where the viscous-elastic and acoustic time and length scales are identical. In addition, for $\lambda/r^{(1)} = 1$ and 1.5 the number of zeros of $\langle U_\theta \rangle$ is identical to the number of extremum points of P (for $0° < \theta < 180°$). However, for $\lambda/r^{(1)} = 0.5$, the first zero of $\langle U_\theta \rangle$ is at $\theta \approx 80°$ and there are several small extremum points of P without a corresponding zero of $\langle U_\theta \rangle$. This indicates that $\langle U_\theta \rangle$ at the backward surface of the sphere (relative to the direction of the impinging wave) is dominated by θ-displacement of the elastic shell and not by the pressure gradient.

Figure 3 presents the average absolute magnitude of the displacements of the outer shell in the radial and tangential directions for a fully elastic sphere (grey lines) and

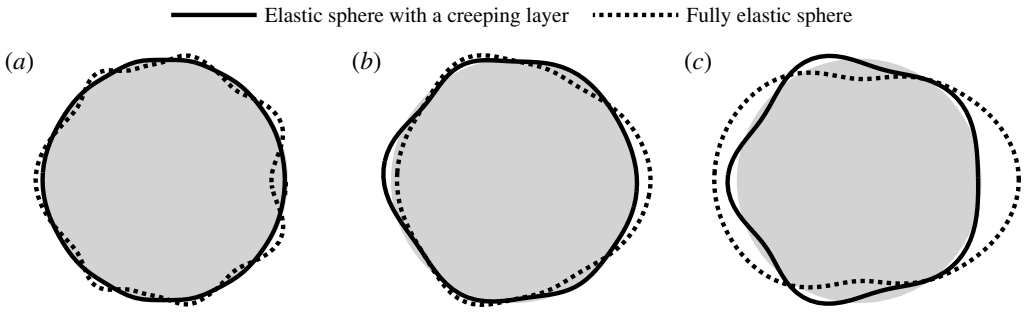

FIGURE 4. The displacement modes for wavelengths of $\lambda/r^{(1)} = 0.5$ (a), 1 (b) and 1.5 (c). The grey circles are the sphere at rest. Dotted lines denote a fully elastic sphere and the smooth lines denote the elastic sphere with an embedded creeping layer.

an elastic sphere containing a thin creeping layer (black lines). The properties of the sphere are identical to the case presented in figure 2. The multiple peaks presented correspond to resonance frequencies of the fully elastic sphere. The effect of the thin creeping layer is clearly significant, and effectively eliminates the fluctuations in the radial displacements of the elastic sphere as a function of the wavelength of the impinging acoustic plane wave. In addition, while no tangential displacements occur for a fully elastic sphere, the creeping layer creates significant tangential displacements, which are similar in magnitude to the radial deflections. Figure 4 supplements figure 3 and presents a more detailed description of the displacements of the outer surface of the sphere for a given wavelength. Figure 4(a–c) presents wavelengths of $\lambda/r^{(1)} = 0.5$, 1 and 1.5, respectively. For all wavelengths, in accordance with results of figure 3, the amplitude of the displacements is significantly reduced. In addition, for $\lambda/r^{(1)} = 1$ and 1.5, additional maxima points of the deflection field are created due to the embedded creeping layer.

Figure 5 presents the effect of the creeping fluid layer on the target strength T_s of the sphere. The target strength, measured in decibels, represents acoustic visibility and following common practice is defined here by

$$T_S = 20 \log_{10} \left| \frac{p_s(r = r^{(3)}, \theta = 180^\circ)}{p_a} \right|. \tag{4.2}$$

The total scattered pressure in the external acoustic fluid $p_s^{(4)} = p_r^{(4)} + p_e^{(4)}$ is the sum of the pressure reflected from a rigid sphere $p_r^{(4)}$ (3.2) and the additional pressure due to elastic displacements of the sphere, $p_e^{(4)}$, given by

$$p_e^{(4)} = \rho c^{(4)} \omega \sum_{n=0}^{\infty} \left(\frac{\mathrm{h}_n(kr^{(3)})}{\mathrm{h}_n'(kr^{(3)})} \right) d_{r,n}^{(3)} L_n(\cos(\theta)). \tag{4.3}$$

Figure 5(a) compares target strength (defined by (4.2)) of a fully elastic sphere (grey line) with an elastic sphere with a viscous layer (black line) versus the scaled wavelength of the impinging plane wave. All of the physical and geometric parameters are identical to these used in figure 2, with the exception of $\mu^{(2)}$, which is defined by setting the ratio $t^*/t_a = \mu^{(2)} c^{(4)} / (\varepsilon^{(1)})^3 \varepsilon^{(2)} \lambda^{(3)} r^{(1)} = 1$. The viscous layer significantly reduces the fluctuations of target strength with the wavelength $\lambda/r^{(1)}$. The difference

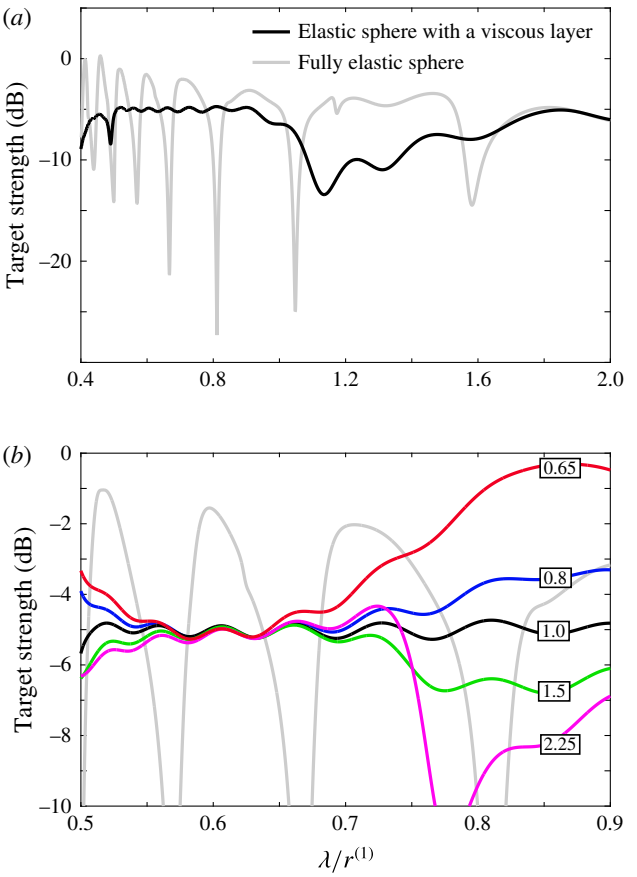

FIGURE 5. (Colour online) Target strength (defined in (4.2)) versus scaled wavelength of the impinging acoustic wave $\lambda/r^{(1)}$. (*a*) The target strength of an elastic sphere with an embedded viscous layer and $t^*/t_a = 1$ (black line) and the target strength of a fully elastic sphere (grey line). (*b*) A close-up of wavelength in the region $0.5 \leqslant \lambda/_r \leqslant 0.9$ with additional values of t^*/t_a.

between the minimal and maximal values of the target strength is reduced from $\approx$ 27 dB (from ≈ -27 to ≈ 0.25) for the fully elastic sphere to ≈ 8.7 dB (from ≈ -13.4 to ≈ -4.7) for the sphere with a creeping layer. Furthermore, for wavelengths in the range $0.5 \leqslant \lambda/r^{(1)} \leqslant 0.9$ the fluctuations are under 1 dB and the target strength is only weakly dependent on the wavelength $\lambda/r^{(1)}$. As the impinging wavelength increases, the effect of the creeping layer is diminished, becoming negligible for $\lambda/r^{(1)} \approx 2$. This occurs since the sphere experiences spatially uniform temporally oscillating pressure at the limit of large wavelengths, which involves no viscous flow in region 2 and is described by the fully elastic $n = 0$ mode (see (3.10)).

Figure 5(*b*) is a close-up of figure 4(*a*) for the region $0.5 \leqslant \lambda/r^{(1)} \leqslant 0.9$ and compares several values of $t^*/t_a = \mu^{(2)} c^{(4)}/(\varepsilon^{(1)})^3 \varepsilon^{(2)} \lambda^{(3)} r^{(1)}$ denoted by markers within the figure. While a region of stability of target strength is evident for all values of t^*/t_a, the wavelength range of this region is maximal for $t^*/t_a = 1$. Viscosity may be expected to have maximal effect for $t^*/t_a \approx 1$ since for $t^*/t_a \gg 1$ the viscous layer does not have sufficient time to react to the acoustic oscillations. For the opposite

case of $t^*/t_a \ll 1$, the viscous layer will be in a quasi-steady state and will have nearly uniform pressure $p^{(2)} \approx \text{const}$.

5. Concluding remarks

This work examined the dynamics of an acoustic plane wave impinging on the surface of a sphere with an embedded creeping layer, focusing on micro-configurations with similar viscous-elastic and acoustic time and length scales. By expanding the linearized spherical Reynolds equation into the relevant spectral series solution for the hyperbolic elastic regions, a global stiffness matrix of the layered elastic sphere was obtained.

As expected, the results showed that both the pressure and velocity within the creeping layer are maximal near the region on which the plane wave impinges. In addition, the maximal pressure difference induced by the acoustic wave on the creeping region 2 was shown to occur for $\lambda/r^{(1)} = 1$, where the viscous-elastic and acoustic regions have identical time and length scales. Comparing an elastic sphere with an embedded creeping layer to a fully elastic sphere, a significant reduction in magnitude and fluctuations (with regard to wavelength) are observed for both the displacements of the solid and the target strength of the sphere. This effect was most significant for $\lambda/r^{(1)} = 1$.

The physical regime examined in this work required similar characteristic acoustic and viscous-elastic time- and length scales, as well as negligible inertial effects in the creeping region 2 and negligible viscous effects in the acoustic region 4. Order-of-magnitude analysis yielded that the region of validity of this physical regime is limited to micro-configurations involving highly viscous fluids. Extension to greater length scales may be obtained by combining multiple spheres, which may be viewed as a metamaterial. Alternatively, a similar physical regime may be examined in porous structures, which commonly involve micrometre-sized pores.

Appendix. Components of the global stiffness matrix

For completeness, we list here the components of the global stiffness matrix (3.9) representing regions 1, 3 and 4 (see Skelton & James 1997). We denote j_n, y_n and h_n as the spherical Bessel function of the first kind, the spherical Bessel function of the second kind, and the spherical Hankel function of the first kind, respectively.

In region 4, we define $k^{(4)} = \omega/c^{(4)}$, where $c^{(4)}$ is the speed of sound. In § 4 the value of $c^{(4)} = 1480$ m s^{-1} is used, representing sea water, and the relevant component in (3.10) is

$$f_{11} = \rho^{(4)} c^{(4)} \omega \left(\frac{\mathrm{h}_n(k^{(4)} r^{(3)})}{\mathrm{h}_n'(k^{(4)} r^{(3)})} \right). \tag{A 1}$$

For the elastic regions $M = 1$ and $M = 3$ we define $k_s^{(M)} = \omega/c_s^{(M)}$ and $k_l^{(M)} = \omega/c_l^{(M)}$, where $c_s^{(M)}$ and $c_l^{(M)}$ are speeds of pure transverse and longitudinal waves in the elastic solid, respectively. In § 4 the values of $c_s = 3130$ m s^{-1} and $c_l = 5760$ m s^{-1} are used, corresponding to steel. The coefficient matrix of elastic region 3 is given by

$$[\boldsymbol{e}] = [\boldsymbol{I}_0][\boldsymbol{a}][\boldsymbol{b}]^{-1}, \tag{A 2}$$

where $\boldsymbol{I}_0$ is a diagonal matrix with diagonal values of $[1, 1, -1, -1]$ required in order to adjust for directionality in the boundary conditions. The components of matrix $\boldsymbol{a}$

are

$$a_{11} = \lambda^{(3)} \left\{ k_l^2 \mathrm{j}_n''(k_l r^{(3)}) + \frac{2k_l^2 \mathrm{j}_n'(k_l r^{(3)})}{r^{(3)}} - \frac{n(n+1)\mathrm{j}_n(k_l r^{(3)})}{(r^{(3)})^2} \right\} + 2\mu^{(3)} k_l^2 \mathrm{j}_n''(k_l r^{(3)}), \quad \text{(A 3)}$$

$$a_{12} = \lambda \left\{ k_l^2 \mathrm{y}_n''(k_l r^{(3)}) + \frac{2k_l^2 \mathrm{y}_n'(k_l r^{(3)})}{r^{(3)}} - \frac{n(n+1)\mathrm{y}_n(k_l r^{(3)})}{(r^{(3)})^2} \right\} + 2\mu^{(3)} k_l^2 \mathrm{y}_n''(k_l r^{(3)}), \quad \text{(A 4)}$$

$$a_{13} = -2\mu^{(3)} n(n+1) \left\{ \frac{k_s \mathrm{j}_n'(k_s r^{(3)})}{r^{(3)}} - \frac{\mathrm{j}_n(k_s r^{(3)})}{(r^{(3)})^2} \right\}, \quad \text{(A 5)}$$

$$a_{14} = -2\mu^{(3)} n(n+1) \left\{ \frac{k_s \mathrm{y}_n'(k_s r^{(3)})}{r^{(3)}} - \frac{\mathrm{y}_n(k_s r^{(3)})}{(r^{(3)})^2} \right\}, \quad \text{(A 6)}$$

$$a_{21} = 2\mu^{(3)} \left[\frac{k_l \mathrm{j}_n'(k_l r^{(3)})}{r^{(3)}} - \frac{\mathrm{j}_n(k_l r^{(3)})}{(r^{(3)})^2} \right], \quad a_{22} = 2\mu^{(3)} \left[\frac{k_l \mathrm{y}_n'(k_l r^{(3)})}{r^{(3)}} - \frac{\mathrm{y}_n(k_l r^{(3)})}{(r^{(3)})^2} \right], \quad \text{(A 7}a,b\text{)}$$

$$a_{23} = \mu^{(3)} \left[\frac{2\mathrm{j}_n(k_s r^{(3)})}{(r^{(3)})^2} - k_s^2 \mathrm{j}_n''(k_s r^{(3)}) - \frac{n(n+1)\mathrm{j}_n(k_s r^{(3)})}{(r^{(3)})^2} \right], \quad \text{(A 8)}$$

$$a_{24} = \mu^{(3)} \left[\frac{2\mathrm{y}_n(k_s r^{(3)})}{(r^{(3)})^2} - k_s^2 \mathrm{y}_n''(k_s r^{(3)}) - \frac{n(n+1)\mathrm{y}_n(k_s r^{(3)})}{(r^{(3)})^2} \right], \quad \text{(A 9)}$$

$$a_{31} = \lambda^{(3)} \left\{ k_l^2 \mathrm{j}_n''(k_l r^{(2)}) + \frac{2k_l^2 \mathrm{j}_n'(k_l r^{(2)})}{r^{(2)}} - \frac{n(n+1)\mathrm{j}_n(k_l r^{(2)})}{(r^{(2)})^2} \right\} + 2\mu^{(3)} k_l^2 \mathrm{j}_n''(k_l r^{(2)}), \quad \text{(A 10)}$$

$$a_{32} = \lambda^{(3)} \left\{ k_l^2 \mathrm{y}_n''(k_l r^{(2)}) + \frac{2k_l^2 \mathrm{y}_n'(k_l r^{(2)})}{r^{(2)}} - \frac{n(n+1)\mathrm{y}_n(k_l r^{(2)})}{r^{(2)}} \right\} + 2\mu^{(3)} k_l^2 \mathrm{y}_n''(k_l r^{(2)}), \quad \text{(A 11)}$$

$$a_{33} = -2\mu^{(3)} n(n+1) \left\{ \frac{k_s \mathrm{j}_n'(k_s r^{(2)})}{r^{(2)}} - \frac{\mathrm{j}_n(k_s r^{(2)})}{(r^{(2)})^2} \right\}, \quad \text{(A 12)}$$

$$a_{34} = -2\mu^{(3)} n(n+1) \left\{ \frac{k_s \mathrm{y}_n'(k_s r^{(2)})}{r^{(2)}} - \frac{\mathrm{y}_n(k_s r^{(2)})}{(r^{(2)})^2} \right\}, \quad \text{(A 13)}$$

$$a_{41} = 2\mu^{(3)} \left[\frac{k_l \mathrm{j}_n'(k_l r^{(2)})}{r^{(2)}} - \frac{\mathrm{j}_n(k_l r^{(2)})}{(r^{(2)})^2} \right], \quad a_{42} = 2\mu^{(3)} \left[\frac{k_l \mathrm{y}_n'(k_l r^{(2)})}{r^{(2)}} - \frac{\mathrm{y}_n(k_l r^{(2)})}{(r^{(2)})^2} \right], \quad \text{(A 14}a,b\text{)}$$

$$a_{43} = \mu^{(3)} \left[\frac{2\mathrm{j}_n(k_s r^{(2)})}{(r^{(2)})^2} - k_s^2 \mathrm{j}_n''(k_s r^{(2)}) - \frac{n(n+1)\mathrm{j}_n(k_s r^{(2)})}{(r^{(2)})^2} \right], \quad \text{(A 15)}$$

$$a_{44} = \mu^{(3)} \left[\frac{2\mathrm{y}_n(k_s r^{(2)})}{(r^{(2)})^2} - k_s^2 \mathrm{y}_n''(k_s r^{(2)}) - \frac{n(n+1)\mathrm{y}_n(k_s r^{(2)})}{(r^{(2)})^2} \right], \quad \text{(A 16)}$$

and the components of matrix $\boldsymbol{b}$ are

$$b_{11} = k_l \mathrm{j}_n'(k_l r^{(3)}), \quad b_{12} = k_l \mathrm{y}_n'(k_l r^{(3)}), \quad b_{13} = -\frac{n(n+1)}{r^{(3)}} \mathrm{j}_n(k_s r^{(3)}), \quad \text{(A 17}a\text{–}c\text{)}$$

$$b_{14} = -\frac{n(n+1)}{r^{(3)}} \mathrm{y}_n(k_s r^{(3)}), \quad b_{21} = \frac{\mathrm{j}_n(k_l r^{(3)})}{r^{(3)}}, \quad b_{22} = \frac{\mathrm{y}_n(k_l r^{(3)})}{r^{(3)}}, \quad \text{(A 18}a\text{–}c\text{)}$$

$$b_{23} = -\left(\frac{\mathrm{j}_n(k_s r^{(3)})}{r^{(3)}} + k_s \mathrm{j}_n'(k_s r^{(3)})\right), \quad b_{24} = -\left(\frac{\mathrm{y}_n(k_s r^{(3)})}{r^{(3)}} + k_s \mathrm{y}_n'(k_s r^{(3)})\right), \quad \text{(A 19}a,b\text{)}$$

$$b_{31} = k_l \mathrm{j}_n'(k_l r^{(2)}), \quad b_{32} = k_l \mathrm{y}_n'(k_l r^{(2)}), \quad b_{33} = -\frac{n(n+1)}{r^{(2)}} \mathrm{j}_n(k_s r^{(2)}), \quad \text{(A 20}a\text{–}c\text{)}$$

$$b_{34} = -\frac{n(n+1)}{r^{(2)}} \mathrm{y}_n(k_s r^{(2)}), \quad b_{41} = \frac{\mathrm{j}_n(k_l r^{(2)})}{r^{(2)}}, \quad b_{42} = \frac{\mathrm{y}_n(k_l r^{(2)})}{r^{(2)}}, \quad \text{(A 21}a\text{–}c\text{)}$$

$$b_{43} = -\left(\frac{\mathrm{j}_n(k_s r^{(2)})}{r^{(2)}} + k_s \mathrm{j}_n'(k_s r^{(2)})\right), \quad b_{44} = -\left(\frac{\mathrm{y}_n(k_s r^{(2)})}{r^{(2)}} + k_s \mathrm{y}_n'(k_s r^{(2)})\right). \quad \text{(A 22}a,b\text{)}$$

The stiffness matrix of the interior elastic sphere (region 1) is given by

$$[\boldsymbol{g}] = [\boldsymbol{s}][\boldsymbol{t}]^{-1}, \quad \text{(A 23)}$$

where the components of the matrix $\boldsymbol{s}$ are

$$s_{11} = \lambda^{(1)} \left[k_l^2 \mathrm{j}_n''(k_l r^{(1)}) + \frac{2k_l^2 \mathrm{j}_n'(k_l r^{(1)})}{r^{(1)}} - \frac{n(n+1)\mathrm{j}_n(k_l r^{(1)})}{(r^{(1)})^2}\right] + 2\mu^{(1)} k_l^2 \mathrm{j}_n''(k_l r^{(1)}), \quad \text{(A 24)}$$

$$s_{12} = -2\mu^{(1)} n(n+1) \left[\frac{k_s \mathrm{j}_n'(k_s r^{(1)})}{r^{(1)}} - \frac{\mathrm{j}_n(k_s r^{(1)})}{(r^{(1)})^2}\right], \quad \text{(A 25)}$$

$$s_{21} = 2\mu^{(1)} \left[\frac{k_l \mathrm{j}_n'(k_l r^{(1)})}{r^{(1)}} - \frac{\mathrm{j}_n(k_l r^{(1)})}{(r^{(1)})^2}\right], \quad \text{(A 26)}$$

$$s_{22} = \mu^{(1)} \left[\frac{2\mathrm{j}_n(k_s r^{(1)})}{(r^{(1)})^2} - k_s^2 \mathrm{j}_n''(k_s r^{(1)}) - \frac{n(n+1)\mathrm{j}_n(k_s r^{(1)})}{(r^{(1)})^2}\right], \quad \text{(A 27)}$$

and the components of the matrix $\boldsymbol{t}$ are

$$t_{11} = k_l \mathrm{j}_n'(k_l r^{(1)}), \quad t_{12} = -\frac{n(n+1)}{r^{(1)}} \mathrm{j}_n(k_s r^{(1)}), \quad \text{(A 28}a,b\text{)}$$

$$t_{21} = \frac{\mathrm{j}_n(k_l r^{(1)})}{r^{(1)}}, \quad t_{22} = -\left[\frac{\mathrm{j}_n(k_s r^{(1)})}{r^{(1)}} + k_s \mathrm{j}_n'(k_s r^{(1)})\right]. \quad \text{(A 29}a,b\text{)}$$

REFERENCES

ARCO, R. M., VÉLEZ-CORDERO, J. R., LAUGA, E. & ZENIT, R. 2014 Viscous pumping inspired by flexible propulsion. *Bioinspir. Biomim.* **9** (3), 036007.

BALMFORTH, N. J., CRASTER, R. V. & HEWITT, I. J. 2015 The speed of an inclined ruck. *Proc. R. Soc. Lond.* A **471**, 20140740.

BOWEN, P. T. & URZHUMOV, Y. A. 2016 Three forms of omnidirectional acoustic invisibility engineered using fast elastodynamic transfer-matrix method. *J. Opt.* **18** (4), 044025.

CAMALET, S. & JÜLICHER, F. 2000 Generic aspects of axonemal beating. *New J. Phys.* **2**, 24.1–24.23.

CANIC, S. & MIKELIC, A. 2003 Effective equations modeling the flow of a viscous incompressible fluid through a long elastic tube arising in the study of blood flow through small arteries. *SIAM J. Appl. Dyn. Syst.* **2** (3), 431–463.

CHAUHAN, A. & RADKE, C. J. 2002 Settling and deformation of a thin elastic shell on a thin fluid layer lying on a solid surface. *J. Colloid Interface Sci.* **245** (1), 187–197.

DUCHEMIN, L. & VANDENBERGHE, N. 2014 Impact dynamics for a floating elastic membrane. *J. Fluid Mech.* **756**, 544–554.

DUPRAT, C. & STONE, H. A. 2015 *Fluid–Structure Interactions in Low-Reynolds-Number Flows*. Royal Society of Chemistry.

ELBAZ, S. B. & GAT, A. D. 2014 Dynamics of viscous liquid within a closed elastic cylinder subject to external forces with application to soft robotics. *J. Fluid Mech.* **758**, 221–237.

FARAN, J. J. JR 1951 Sound scattering by solid cylinders and spheres. *J. Acoust. Soc. Am.* **23** (4), 405–418.

GUILD, M. D., ALU, A. & HABERMAN, M. R. 2011 Cancellation of acoustic scattering from an elastic sphere. *J. Acoust. Soc. Am.* **129** (3), 1355–1365.

GUILD, M. D., HICKS, A. J., HABERMAN, M. R., ALÙ, A. & WILSON, P. S. 2015 Acoustic scattering cancellation of irregular objects surrounded by spherical layers in the resonant regime. *J. Appl. Phys.* **118** (16), 164903.

HAN, Z., TAO, C., ZHOU, D., SUN, Y., ZHOU, C., REN, Q. & ROBERTS, C. J. 2014 Air puff induced corneal vibrations: theoretical simulations and clinical observations. *J. Refract. Surg.* **30** (3), 208–213.

HEIL, M. 1997 Stokes flow in collapsible tubes – computation and experiment. *J. Fluid Mech.* **353**, 285–312.

HEWITT, I. J., BALMFORTH, N. J. & DE BRUYN, J. R. 2015 Elastic-plated gravity currents. *Eur. J. Appl. Maths* **26** (01), 1–31.

HOSOI, A. E. & MAHADEVAN, L. 2004 Peeling, healing, and bursting in a lubricated elastic sheet. *Phys. Rev. Lett.* **93** (13), 137802.

HOWELL, P., KOZYREFF, G. & OCKENDON, J. 2009 *Applied Solid Mechanics*. Cambridge University Press.

HUANG, X., ZHONG, S. & LIU, X. 2014 Acoustic invisibility in turbulent fluids by optimised cloaking. *J. Fluid Mech.* **749**, 460–477.

LISTER, J. R., PENG, G. G. & NEUFELD, J. A. 2013 Viscous control of peeling an elastic sheet by bending and pulling. *Phys. Rev. Lett.* **111** (15), 154501.

LOGAN, N. A. 1965 Survey of some early studies of the scattering of plane waves by a sphere. *Proc. IEEE* **53** (8), 773–785.

LOVE, A. E. H. 1927 *A Treatise on the Mathematical Theory of Elasticity*, vol. 1. Cambridge University Press.

LOWE, T. W. & PEDLEY, T. J. 1995 Computation of Stokes flow in a channel with a collapsible segment. *J. Fluids Struct.* **9** (8), 885–905.

MCEWAN, A. D. & TAYLOR, G. I. 1966 The peeling of a flexible strip attached by a viscous adhesive. *J. Fluid Mech.* **26** (01), 1–15.

SKELTON, E. A. & JAMES, J. H. 1997 *Theoretical Acoustics of Underwater Structures*. Imperial College Press.

TONY, S. Y., LAUGA, E. & HOSOI, A. E. 2006 Experimental investigations of elastic tail propulsion at low Reynolds number. *Phys. Fluids* **18** (9), 091701.

TORRENT, D. & SÁNCHEZ-DEHESA, J. 2008 Acoustic cloaking in two dimensions: a feasible approach. *New J. Phys.* **10** (6), 063015.

WIGGINS, C. H. & GOLDSTEIN, R. E. 1998 Flexive and propulsive dynamics of elastica at low Reynolds number. *Phys. Rev. Lett.* **80** (17), 3879.